Journal of Simulation and Analysis of Novel Technologies in Mechanical Engineering
17 (3) (2025) 0063~0085
DOI 10.71939/jsme.2025.1216647

Research article

Enhanced flow control in electromechanically driven valveless micropumps: from structural design insights to multi-core actuation dynamics

Parisa Mahmoudi*[1,2]

[1]*Assistant Professor, Department of Electrical Engineering, Payame Noor University, Tehran, Iran*
[2]*Microsystem Fabrication Laboratory, Department of Electrical and Computer Engineering, University of Tabriz, Tabriz, Iran*

*parisamahmoudi@pnu.ac.ir

(Manuscript Received --- 01 Sep. 2025; Revised --- 02 Dec. 2025; Accepted --- 21 Dec. 2025)

Abstract

This study presents a fully cylindrical piezoelectric micropump for precise fluid handling in microfluidic applications. The design integrates a ring-shaped piezoelectric actuator with a flexible membrane above a cylindrical fluid chamber. Under sinusoidal actuation, the actuator induces vertical membrane oscillations that generate pressure gradients, and drive directional fluid transport. Simulation results show that applying a 0.2V/μm electric field yields an accumulated flow volume of 1.3197μL per cycle, with peak inlet and outlet flow rates reaching approximately 0.038mL/s. Parametric analyses reveal that increasing the number of piezoelectric layers at constant voltage, significantly boosts flow rates due to enhanced mechanical stiffness and actuation force. Additionally, expanding the inner radius of the actuator improves membrane leverage and peak displacement. In contrast, increasing the outer radius distributes force over a larger area, which enhances net volume flow despite reduced peak deflection. Larger membrane radii amplify volumetric displacement through increased surface area. However, enlarging inlet/outlet port radii reduces flow rates due to diminished pressure buildup and weakened passive flow rectification. Frequency sweep analysis identifies a resonant frequency at 940Hz, where maximum flow of 4.1528μL is achieved. Furthermore, multi-core actuator configurations composed of several narrower piezoelectric rings, demonstrate tunable pumping characteristics that depend on their spatial arrangement. These findings underscore the importance of geometric and electrical optimization in piezoelectric micropump design. They provide a robust framework for enhancing performance and controllability in precise microfluidic applications.

Keywords: Micropump, Piezoelectric, Actuator, Membrane, Flow Rate, Flow Volume, Multi-core.

1- Introduction

Microfluidics is a rapidly evolving field that deals with the manipulation of fluids at the microscale, typically within channels ranging from tens to hundreds of micrometers in diameter. This technology underpins a wide array of applications, including biomedical diagnostics, drug delivery, chemical synthesis, and environmental monitoring. The miniaturization of fluidic systems offers advantages such as reduced reagent

consumption, faster reaction times, and enhanced portability. However, the precise control and transport of fluids within these confined geometries require specialized components, among which micropumps play a pivotal role [1-3].

Micropumps are essential actuators in microfluidic platforms, that enable controlled fluid movement without relying on bulky external equipment. Their integration into lab-on-chip systems allows for autonomous operation, making them indispensable in point-of-care diagnostics and wearable devices [4-6]. A micropump is a miniaturized device designed to generate and regulate fluid flow. It typically consists of a pumping chamber, an actuator, and flow-directing elements such as valves or nozzles. The actuator drives the movement of a diaphragm or membrane, which displaces fluid in a cyclical manner, and produces a net flow [7,8].

Micropumps can be broadly classified based on their actuation mechanisms into mechanical and non-mechanical types [3, 9-12]. Mechanical micropumps use moving parts such as diaphragms, pistons, or rotors, and are often driven by piezoelectric, electrostatic, thermopneumatic, or electromagnetic forces. Among these, piezoelectric micropumps are widely studied due to their fast response, high precision, and compatibility with silicon-based fabrication [13-15]. Recent reviews have highlighted the state-of-the-art in piezoelectric micropump technology, emphasizing both design evolution and biomedical applications [16]. Non-mechanical micropumps, on the other hand, rely on phenomena such as electroosmotic flow, magnetohydrodynamics, or surface tension gradients, and typically offer simpler designs with fewer moving parts [3, 17-19].

Further classification can be made based on valve configuration: valved micropumps use check valves or flap valves to direct flow, while valveless designs rely on asymmetric geometries or nozzle-diffuser elements to achieve unidirectional flow. In the context of numerical modeling, the term valveless refers to the absence of physical valve structures, with flow rectification instead represented through boundary conditions or geometric asymmetry. This distinction ensures that the micropump remains valveless in design, while the simulation framework captures directional flow behavior using mathematical constraints. Each design presents trade-offs in terms of flow rate, pressure generation, power consumption, and fabrication complexity [20-22]. Recent studies have advanced these classifications, where hydraulic amplification-based piezoelectric micropumps have been designed and tested [23], valve-less micropumps generating recirculating flow have been proposed [24], and multi-channel silicon-based micropumps with active valve arrays have been developed [25].

The applications of micropumps span across disciplines. In biomedical engineering, they are used for insulin delivery, microdialysis, and organ-on-chip systems. In chemical analysis, micropumps facilitate sample injection and reagent mixing. Environmental sensors benefit from micropumps for fluid sampling and transport in remote or confined locations. Moreover, micropumps are increasingly integrated into soft robotics and microelectromechanical systems (MEMS), where precise fluid control is essential for

actuation and sensing [26-30]. Recent contributions include the design and simulation of piezoelectric micropumps for drug delivery systems [31], analytical and experimental studies of valveless micropumps with high flowrate and pressure load [32], and demonstrations of high-flow piezoelectric micropumps for miniature liquid cooling [33]. Integrated Multiphysics modeling approaches have also been introduced, underscoring the importance of simulation frameworks in advancing micropump design [34]. Hence, micropumps are foundational components in microfluidic systems, that enable precise and programmable fluid manipulation. Their diverse actuation principles and design architectures allow them to be tailored for specific applications, and make them a subject of ongoing research and innovation in both academia and industry.

In this study, a valveless piezoelectric micropump featuring a fully cylindrical geometry is introduced. Here, valveless emphasizes the absence of mechanical check valves, while the unidirectional flow is achieved through direction-dependent boundary conditions applied in the simulation model. Section 2 describes the structural design, governing equations, boundary conditions and material properties. Section 3 develops a fully parametric framework that systematically investigates the influence of geometric and electrical parameters, enabling optimization strategies that extend beyond current models. The novelty of this work also lies in the adoption of a fully cylindrical micropump architecture, which departs from conventional rectangular or partially cylindrical designs and establishes a new pathway for achieving resonance stability and controllability.

In addition, the concept of multi-core actuation is introduced in this study. it refers to the spatial segmentation of the piezoelectric actuator into multiple concentric and adjacent ring-shaped cores. Unlike conventional layer stacking, where piezoelectric films are vertically superimposed, multi-core segmentation enables independent or collective excitation of narrower rings. The dynamics of this configuration is analyzed in section 4, showing that spatially distributed actuation can be strategically employed as a design tool to tune flow rate and controllability beyond single-core or stacked-layer approaches.

2- Theoretical background

2-1- Micropump geometry and design parameters

The proposed micropump features a ring-shaped piezoelectric actuator positioned above a cylindrical fluid chamber, mechanically coupled to a flexible membrane. The adoption of a fully cylindrical architecture, including the fluid chamber, membrane, actuator, and inlet/outlet configuration, offers both fabrication simplicity and enhanced performance in piezoelectric micropump systems. From a manufacturing standpoint, cylindrical components are inherently compatible with rotary and symmetric microfabrication techniques, reducing alignment errors and simplifying assembly. This geometry also facilitates uniform stress distribution across the piezoelectric membrane, and results in more efficient actuation and consistent fluid displacement. Unlike rectangular chambers, which may introduce corner-induced turbulence and dead zones, the cylindrical design promotes smoother flow dynamics and minimizes energy loss.

Additionally, the radial symmetry of the actuator and membrane ensures optimal resonance behavior. These combined benefits make the cylindrical configuration a compelling choice for high-precision microfluidic applications such as biomedical dosing, inkjet printing, and lab-on-a-chip systems. As illustrated in Fig. 1(a), the complete geometry includes all essential structural components. However, due to the symmetry of the physical system, only half of the domain is modeled to reduce computational complexity while preserving accuracy. Application of a sinusoidal voltage across the piezoelectric actuator induces thickness-direction deformation, resulting in vertical expansion or contraction depending on the polarity of the applied field. This vertical displacement drives the membrane to oscillate up and down. So, its motion generates pressure variations within the fluid chamber. These pressure gradients initiate a pumping cycle, so that fluid is drawn in from the inlet when the membrane moves upward, and expelled through the outlet when it moves downward. Importantly, the flow rate is governed not by the membrane's static position but by its velocity. Maximum inlet flow occurs when the membrane crosses its neutral position moving upward, while maximum outlet flow corresponds to downward motion through the same neutral point. This dynamic behavior reflects the phase relationships between voltage, displacement, and flow.

The simulation domain focuses on this half-section, capturing the essential fluid-structure interactions while maintaining computational efficiency (Fig. 1(b)). Fig. 1(c) highlights the distinct components of the micropump, including the actuator, membrane, fluid domain, and inlet/outlet channels. The specific dimensions and geometric parameters used in the design are summarized in Table 1.

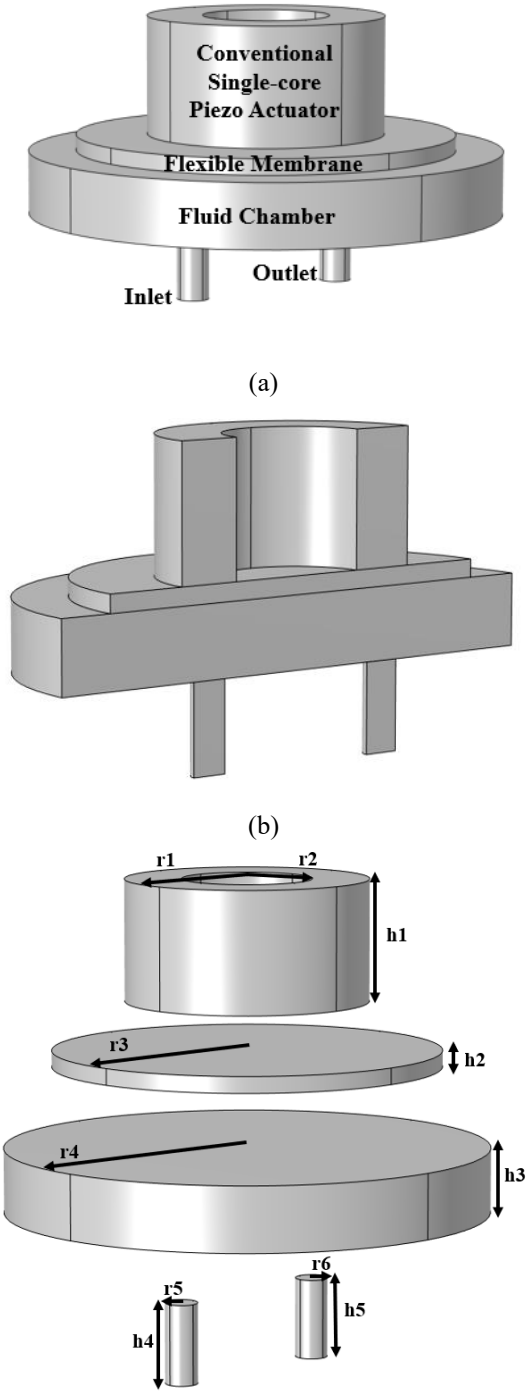

Fig. 1 Illustration of (a) the complete geometry of the micropump with labeled parts, (b) the half-domain used for simulation, and (c) the distinct components of the micropump. The piezoelectric actuator shown here represents the conventional single-core configuration used as the baseline design.

Table 1: Dimensions for the proposed micropump design

parameter	value	definition
r1	7.5mm	Outer Radius of Actuator
r2	4mm	Inner Radius of Actuator
r3	12mm	Radius of Membrane
r4	15mm	Radius of Fluid Chamber
r5	1mm	Fluid Inlet Radius
r6	1mm	Fluid Outlet Radius
h1	7.5mm	Height of Actuator
h2	1mm	Height of Membrane
h3	4mm	Height of Fluid Chamber
h4	5mm	Height of Inlet
h5	5mm	Height of Outlet

2-2- Governing equations of micropump operation

The operation of a piezoelectric micropump is governed by a complex interplay between structural mechanics, electrostatics, and fluid dynamics.

These domains are intrinsically coupled through electromechanical interactions and fluid-structure interfaces. So, a Multiphysics modeling approach is required. The following formulation outlines the fundamental equations that describe the behavior of the whole system.

2-2-1- Structural mechanics and piezoelectric Coupling

The piezoelectric actuator undergoes mechanical deformation in response to an applied electric field. This deformation is transmitted to a flexible membrane, which in turn drives fluid motion within the microchannel. The mechanical response of the solid domain is described by the balance of linear momentum:

$$\nabla.\sigma + F = \rho\frac{\partial^2 u}{\partial t^2} \tag{1}$$

where σ is the stress tensor (Pa), F represents body forces (N/m³), ρ is the material density (kg/m³), and u is the displacement vector (m). The stress tensor is related to the strain and electric field through the constitutive relation for piezoelectric materials [35]:

$$\sigma = C.\varepsilon - e^T.E \tag{2}$$

Here, C is Elastic stiffness matrix (Pa), ε is the strain tensor (unitless), e^T is the transposed piezoelectric coupling matrix (C/m²), and E is the electric field vector (V/m). The strain tensor itself is defined in terms of the displacement gradient:

$$\varepsilon = \frac{1}{2}(\nabla u + (\nabla u)^T) \tag{3}$$

This formulation captures the bidirectional electromechanical coupling (i.e. the electric field induces mechanical strain, and conversely, mechanical deformation generates electric displacement) [17-18, 24-25]. Although the geometric nonlinearity option in COMSOL is enabled, sensitivity checks show that disabling it produces identical results, consistent with the small-strain regime in this study.

2-2-2- Electrostatics in piezoelectric domain

The electrical behavior of the piezoelectric actuator is governed by Gauss's law for electrostatics [17,24], which ensures conservation of electric charge:

$$\nabla.D = \rho_e \tag{4}$$

where D is the electric displacement field (C/m²) and ρ_e is the free charge density (C/m³). The electric displacement is related to the strain and electric field via the constitutive relation:

$$D = e.\varepsilon + \varepsilon_r.E \tag{5}$$

In this expression, e is the piezoelectric coupling matrix (C/m²), and ε_r is the relative permittivity matrix (F/m) of the material. The electric field (V/m) itself is derived from the gradient of the electric potential:

$$E = -\nabla V \tag{6}$$

where V is the scalar electric potential (V) applied across the piezoelectric layer.

2-2-3- Fluid dynamics in the microchannel

The fluid domain, typically consisting of an incompressible Newtonian liquid such as water or a buffer solution, is governed by the Navier-Stokes equations [2-3,17]. These equations describe the conservation of mass and momentum within the microchannel. The continuity equation for incompressible flow is given by:

$$\nabla . v = 0 \tag{7}$$

where v is the fluid velocity vector ($^{m}/_{s}$). The momentum conservation equation is expressed as:

$$\rho\left(\frac{\partial v}{\partial t} + (v.\nabla)v\right) = -\nabla P + \mu\nabla^2 v + f \tag{8}$$

Here, ρ is fluid density ($^{kg}/_{m^3}$), P is the pressure field (Pa), μ is the dynamic viscosity of the fluid ($^{kg}/_{m.s}$), and f represents external forces (N/m³), including those induced by membrane motion.

The interaction between the solid and fluid domains is realized through fluid-structure interaction (FSI) at the membrane-fluid interface. The membrane displacement, driven by the piezoelectric actuator through electromechanical coupling, imposes a time-dependent boundary condition on the fluid domain. This generates pressure gradients that induce flow. At the interface, velocity and stress continuity are enforced.

2-3- Boundary conditions

As discussed, the velocity of the fluid matches the velocity of the membrane at the interface:

$$v_{fluid} = \frac{\partial u_{membrane}}{\partial t} \tag{9}$$

Which is displacement continuity at solid-fluid interface. The normal stress exerted by the fluid equals the stress transmitted by the membrane:

$$\sigma_{fluid}.n = \sigma_{solid}.n \tag{10}$$

Which is stress balance between membrane and fluid. These conditions ensure seamless energy transfer between the domains and accurate modeling of the pumping mechanism.

No-slip condition is applied at the fluid channel walls. This ensures that fluid velocity is zero relative to the wall [17,24].

$$v_{fluid} = 0, at\ channel\ walls \tag{11}$$

To simulate directional flow control in the piezoelectric micropump, no physical check valves are included in the design. Instead, flow rectification is represented numerically through pressure boundary conditions that impose flow-dependent resistance. Rather than modeling valve geometry explicitly, this abstraction introduces a velocity-dependent back pressure at the inlet and outlet boundaries. This provides a simplified representation of geometry-induced flow rectification, where directional resistance replaces the need for physical valves [7, 22-23].

This back pressure is formulated as a normal stress given by:

$$p_0 = A \times \rho \times u_{av}^2 \tag{12}$$

where p_0 is the applied pressure, u_{av} is the average fluid velocity normal to the boundary, ρ is the fluid density, and A is a dimensionless coefficient that varies with flow direction. When the flow aligns with the valve's intended direction (open condition), A is set to a low value and when the flow opposes it (closed condition), A is set high. This effectively mimics the behavior of passive valves like flappers or diaphragms. In simulation, at the inlet, the pressure condition is defined as:

$$\begin{gathered} if(av\_in(w2) > 0, \\ -low\_stress, high\_stress) \\ \times (av\_in(w2))^2 \times av\_in(spf.rho) \end{gathered} \tag{13}$$

In this expression, $av\_in(w2)$ is the average normal velocity at the inlet boundary, and $av\_in(spf.rho)$ is the fluid density at that boundary. The conditional term switches between low and high resistance depending on the flow direction (low resistance for forward flow and high resistance for reverse flow). The product $(av\_in(w2))^2 \times av\_in(spf.rho)$ introduces a realistic dynamic pressure component, ensuring that the applied stress scales with both the velocity and the fluid's physical properties.

At the outlet, the logic is reversed to reflect the opposite valve orientation:

$$\begin{gathered} if(av\_out(w2) < 0, \\ low\_stress, -high\_stress) \\ \times (av\_out(w2))^2 \times av\_out(spf.rho) \end{gathered} \tag{14}$$

Here, $av\_out(w2)$ is the average normal velocity at the outlet boundary, and $av\_out(spf.rho)$ is the corresponding fluid density. The conditional term applies low resistance when fluid exits the domain and high resistance when flow attempts to re-enter. Again, the dynamic pressure term $(av\_out(w2))^2 \times av\_out(spf.rho)$ ensures that the applied stress responds proportionally to the flow intensity and fluid characteristics. So, these expressions enable realistic flow behavior without the need for explicit valve geometry. To maintain numerical stability and achieve physically accurate velocity profiles, a short pipe segment is added at each boundary. This transitional region allows the flow to develop naturally before entering the main domain and ensure smooth distribution of the applied stress. By tuning the stress coefficients, the model can be calibrated to replicate specific valve characteristics with high computational efficiency.

To drive the piezoelectric micropump, a time-dependent voltage is applied at the actuator terminal [18,24-25], defined as:

$$V(t) = V_0 \sin(2\pi f t) \times rm1(\frac{4}{3}ft) \tag{15}$$

where V_0 is the peak voltage amplitude, f is the driving frequency, and $rm1(t)$ is a ramp function that smoothly transitions from zero to one over a specified time interval to smoothly ramp up the sinusoidal drive.

In this model, the peak voltage V_0 is calculated using the relation $V_0 = E_0.t_0.n$, which mirrors the behavior of real multilayer piezoelectric actuators. Here, E_0 is the applied electric field strength, t_0 is the thickness of a single piezoelectric layer, and n is the number of stacked layers. Although the physical structure is simplified in the simulation (treating the actuator as a monolithic piezoelectric

structure), the voltage formulation retains the multilayer logic to ensure that the applied field strength and total actuator thickness are correctly represented. This abstraction allows the model to capture the electrical excitation characteristics of a stacked actuator without explicitly resolving each layer. The stiffness of the thin metal contacts is neglected, and a total potential difference is applied across the actuator. In practice, the required voltage would depend on the individual layer thickness and stack configuration, but this approach provides a computationally efficient approximation of the real device behavior.

The drive voltage is ramped up during the first three-quarters of the actuation period, allowing the system to gradually reach full excitation. This modulation prevents abrupt transients that could cause numerical instability or unrealistic mechanical responses. After the ramp-up phase, a consistent time-periodic flow is quickly established, enabling reliable performance analysis of the micropump.

Fig. 2 shows the individual components, (the sinusoidal waveform, the ramp function, and their product) illustrating the smoothly ramped sinusoidal voltage applied to the terminal. This approach enables stable transient simulation and realistic dynamic behavior of the micropump.

2-4- Material properties

The materials used in this study are selected directly from the COMSOL Multiphysics material library to ensure reproducibility. Three domains are defined: the piezoelectric actuator (PZT), the flexible membrane, and the working fluid (water). For the piezoelectric actuator, COMSOL provides anisotropic elastic, dielectric, and piezoelectric coefficients in matrix form, which are listed in Table 2 [17-18,24-25]. The membrane is modeled as an isotropic elastic material, characterized by its Young's modulus, Poisson's ratio, and density (Table 3) [7,22-23]. The fluid domain is defined as water at room temperature, with density, viscosity, and thermophysical properties taken from the COMSOL database (Table 4) [2,3].

2-5-Fluid-structure interaction coupling

The micropump simulations are performed using COMSOL's Fluid-Structure Interaction (FSI) node, with the coupling option set to Fully Coupled. This corresponds to a two-way FSI scheme, in which structural deformation of the piezoelectric actuator and membrane alters the fluid domain geometry, while the resulting fluid pressure is simultaneously fed back into the structural solver. This bidirectional coupling ensures accurate representation of the dynamic interaction between the solid and fluid domains and confirms the reproducibility of the model setup.

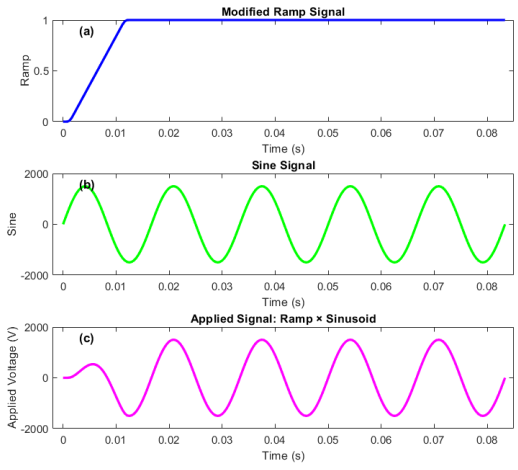

Fig. 2 (a) The ramp function, (b) The basic sinusoidal waveform, (c) Modulated sinusoidal waveform applied to the piezoelectric actuator terminal.

Table 2: Piezoelectric actuator (PZT) properties

property	value	unit	notes
Density (ρ)	7500	kg/m³	Basic
Elasticity matrix (Voigt notation)	{cE11=1.27205×10¹¹, cE12=8.02122×10¹⁰, cE22=1.27205×10¹¹, cE13=8.46702×10¹⁰, cE23=8.46702×10¹⁰, cE33=1.17436×10¹¹, cE44=2.29885×10¹⁰, cE55=2.29885×10¹⁰, cE66=2.34742×10¹⁰}	Pa	Stress–charge form
Piezoelectric coupling matrix (eES, Voigt)	{eES31=−6.62281, eES32=−6.62281, eES33=23.2403, eES24=17.0345, eES15=17.0345}	C/m²	Stress–charge form
Relative permittivity (εrS)	{ε11=1704.4, ε22=1704.4, ε33=1433.6}	—	Stress–charge form
Compliance matrix (sE, Voigt)	{sE11=1.65×10⁻¹¹, sE12=−4.78×10⁻¹², sE22=1.65×10⁻¹¹, sE13=−8.45×10⁻¹², sE23=−8.45×10⁻¹², sE33=2.07×10⁻¹¹, sE44=4.35×10⁻¹¹, sE55=4.35×10⁻¹¹, sE66=4.26×10⁻¹¹}	1/Pa	Strain–charge form
Piezoelectric coupling matrix (dET, Voigt)	{dET31=−2.74×10⁻¹⁰, dET32=−2.74×10⁻¹⁰, dET33=5.93×10⁻¹⁰, dET24=7.41×10⁻¹⁰, dET15=7.41×10⁻¹⁰}	C/N	Strain–charge form
Relative permittivity (εrT)	{ε11=3130, ε22=3130, ε33=3400}	—	Strain–charge form

Table 3: Membrane properties

property	value	unit	notes
Density (ρ)	2320	kg/m³	Basic
Young's modulus (E)	200×10⁶	Pa	Elastic modulus
Poisson's ratio (ν)	0.45	—	Elastic property

Table 4: Fluid (Water) properties

property	value	unit	notes
Density (ρ)	1000	kg/m³	Basic
Dynamic viscosity (μ)	1.0×10⁻³	Pa·s	Basic
Electrical conductivity (σ)	5.5×10⁻⁶	S/m	Basic
Heat capacity at constant pressure (Cp)	~4180	J/(kg·K)	Basic
Thermal conductivity (k)	~0.6	W/(m·K)	Basic

3- Results and Discussion

The simulation study was configured in COMSOL Multiphysics 6.2a to capture the transient behavior of the piezoelectric micropump over multiple actuation cycles. A Time-Dependent Study was employed to follow the time evolution across five drive cycles, with output times defined using the expression range (0,0.025,5)/frequency, ensuring synchronization with the excitation signal. The Include geometric nonlinearity option was activated only as a precautionary solver setting to enhance numerical stability. So, the constitutive law remained linear with the small-strain formulation of Eq. (3).

For enhanced numerical stability and precision, Strict time stepping was selected to minimize interpolation errors during solver iterations. The solver configuration was optimized using a Fully Coupled approach. This method reduces computation time by solving the Multiphysics equations simultaneously rather than sequentially. This setup allowed for efficient and accurate simulation of the coupled electromechanical-fluidic

dynamics. It formed the basis for the parametric analyses presented in the following subsections.

3-1- Mesh independence and numerical validation

A carefully designed meshing strategy is used to resolve the coupled physics of solid mechanics, fluid dynamics, and piezoelectric effects. A swept mesh is applied to the solid domains including membrane and piezoelectric actuator, with quad elements used to improve deformation resolution. For the fluid domain, a boundary layer mesh is added to resolve flow near walls, and triangular elements are used for the bulk fluid mesh.

The mesh is partitioned between solid and fluid regions to enable accurate fluid-structure interaction. Additionally, geometric symmetry is exploited to reduce computational load (Fig. 3(a)).

To validate mesh quality and ensure numerical accuracy, a mesh independence analysis was performed. Simulations were conducted using progressively refined meshes with element counts of 5,769, 10,565, 27,252, 52,926, and 137,194. The resulting volume flow accumulated were compared across these configurations (Fig. 3(b)). Beyond 52,926 elements, the results showed no variation relative to the finest mesh, indicating convergence and mesh independence.

Consequently, the mesh with 52,926 elements was selected for all subsequent simulations, offering an optimal balance between computational efficiency and solution accuracy. To validate the simulation framework, the results obtained from the present numerical method were benchmarked against the numerical data reported by Nabifar et al. [36] for a rectangular micropump.

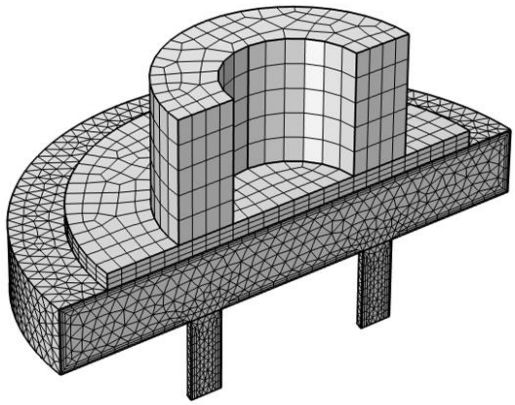

(a)

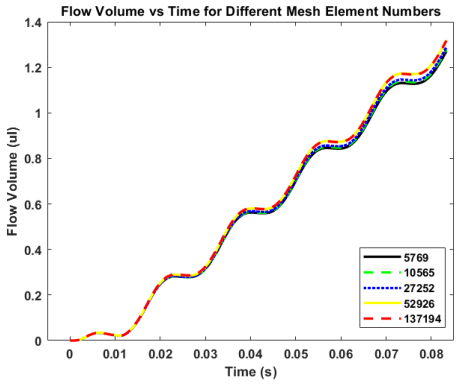

(b)

Fig. 3 (a) Meshing strategy applied to the micropump model. (b) Mesh independence analysis based on accumulated volume flow per cycle across progressively refined meshes, confirming convergence beyond 52,926 elements.

Fig. 4(a) presents the design reconstructed based on their study. Fig. 4(b) compares accumulated flow volume profiles between the current simulation method and the reference data. The simulation parameters were set to an applied voltage of 1500 V, a frequency of 60 Hz, and a total computation time of 0.08 seconds. The profile derived from the present method exhibits strong agreement with that reported by Nabifar et al. [36], thereby confirming the accuracy of the numerical approach. Following this validation, the same set of governing equations and boundary conditions, as detailed in earlier sections, have been employed for all analyses.

3-2-Flow rates and volume conservation

Fig. 5(a) illustrates the inlet and outlet flow rates over time. The plot captures the dynamic fluid exchange driven by membrane motion. Fluid is predominantly drawn in through the inlet (black curve) when the membrane moves upward, with minimal backflow observed at the outlet. Conversely, as the membrane moves downward, fluid is expelled through the outlet (red curve), while the inlet exhibits only minor backflow.

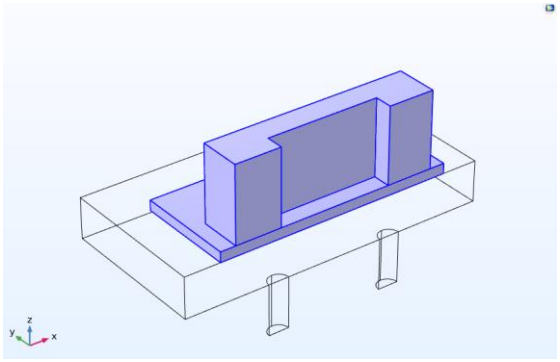

(a)

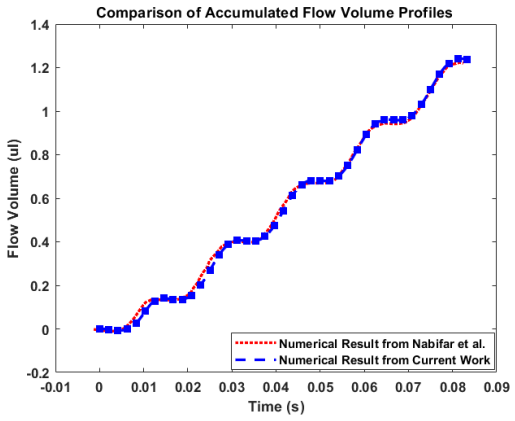

(b)

Fig. 4 Validation of the simulation framework against the study from Nabifar et al. [36] (a) Rectangular micropump design reconstructed based on their reported configuration. (b) Comparison of accumulated flow volume profiles between the present numerical method and the reference data, showing strong agreement and confirming the accuracy of the simulation approach.

These alternating flow patterns reflect the cyclical nature of membrane actuation in response to the applied voltage. At intermediate time points, the flow behavior is governed by the instantaneous membrane velocity and the phase of the driving signal. To verify volume conservation, these flow rates at the inlet and outlet, are summed and compared to the net flow induced by the membrane motion. As shown in Fig. 5(b), the total exchanged flow matches the membrane-driven flow. Their difference is represented by the black line along the time axis, confirming that the system conserves volume throughout the actuation cycle (black zero line).

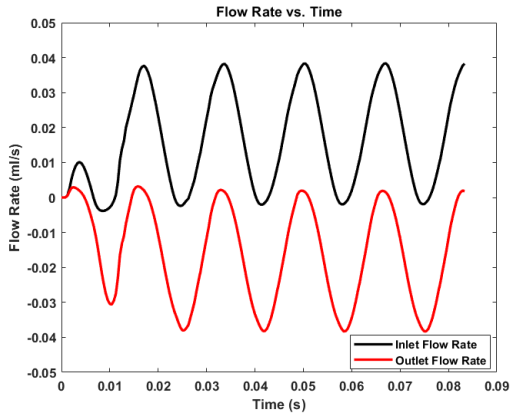

(a)

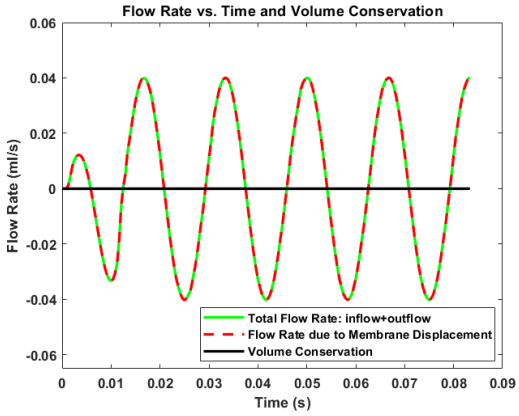

(b)

Fig. 5 (a) Time-resolved flow rates at the inlet and outlet, showing symmetric exchange behavior. (b) Comparison between the total exchanged flow and the membrane-driven flow. The close agreement between the two curves confirms volume conservation, with the black zero line indicating no net fluid change over time.

Fig. 6 displays the velocity fields of the fluid and solid domains at selected time

points within one actuation cycle (0.025s, 0.029s, 0.033s, and 0.0375s), plotted on the symmetry plane. The velocity magnitudes are visualized as solid.vel/1[mm/s] and spf.U/1[mm/s] expressions for the solid and fluid respectively. This approach allows clear representation of both low and high velocity regions at the same time. Overlaid arrow plots indicate the direction of membrane displacement and fluid motion. These snapshots illustrate the dynamic coupling between membrane deformation and fluid exchange. As the membrane oscillates, its motion drives fluid from the inlet to the outlet, with the direction and magnitude of flow varying throughout the cycle. The visual alignment of solid and fluid velocity vectors confirms the effectiveness of the piezoelectric actuation in generating net flow through the chamber.

At 0.025s, the velocity field reveals outflow through the outlet, indicated by positive velocity magnitudes and outward-directed vectors. Simultaneously, a slight backflow at the inlet is observed, characterized by downward velocity arrows. At 0.029s and 0.0375s, the flow distribution becomes more balanced. Both inlet and outlet exhibit comparable magnitudes and directions, suggesting a transitional phase in the actuation cycle where the membrane motion drives fluid symmetrically across the chamber. At 0.0333s, the velocity vectors at the inlet point inward with positive magnitudes, confirming a suction-driven inflow. At the same time, the outlet displays a minor reverse flow, indicating a brief backflow phase. These temporal snapshots underscore the cyclic nature of the piezoelectric actuation, where alternating membrane deformation induces directional fluid transport. The interplay between suction and expulsion phases ensures net flow over time, with transient backflows serving as part of the dynamic equilibrium.

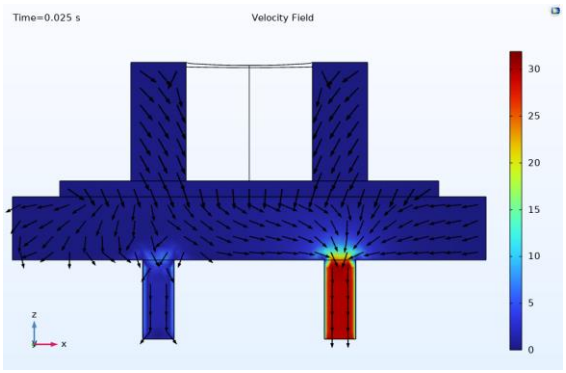

(a)

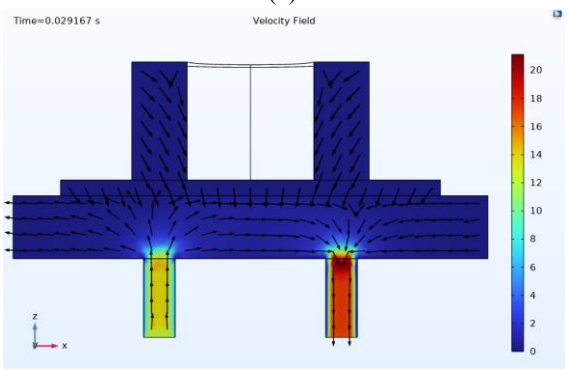

(b)

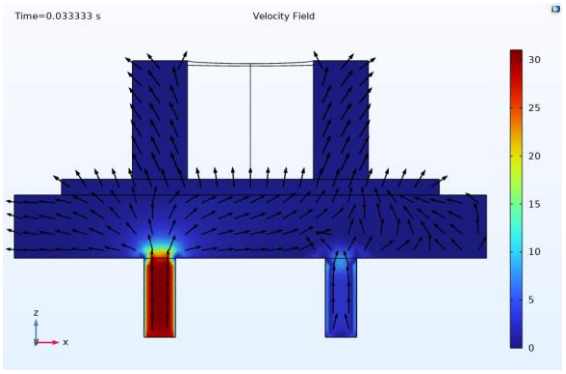

(c)

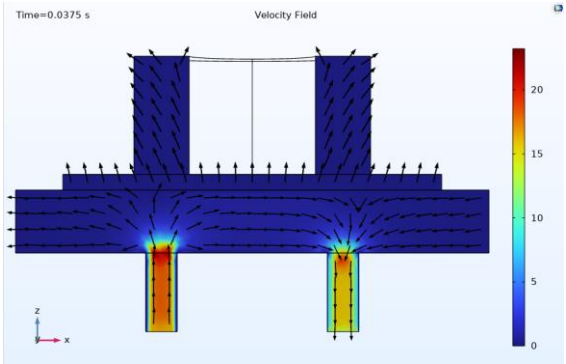

(d)

Fig. 6 Velocity fields at (a) the expulsion phase, (b) intermediate time point with simultaneous inflow

and outflow, (c) the suction phase, and (d) the next intermediate point, show membrane-driven fluid motion during one actuation cycle of [0.025s-0.042s]. Arrows and magnitudes reveal alternating suction and expulsion phases, confirming effective piezoelectric flow generation.

Fig. 7 illustrates the time evolution of the cumulative fluid volumes entering and exiting the micropump. The plot captures the transient flow behavior induced by cyclic membrane actuation. These curves are obtained by integrating the instantaneous flow rates at the boundaries using a global ordinary differential equation. This approach allows continuous tracking of the total fluid volume transported through each port from the start of the simulation. The periodic nature of the actuation cycle is reflected in the alternating slopes of the curves. During the suction phase, membrane upward contraction generates inflow, resulting in an increase in the inlet volume. However, during the expulsion phase, membrane downward expansion drives outflow, causing the outlet volume to surpass the inlet. Intersections between the inlet and outlet curves correspond to instants when the net fluid volume within the chamber is zero, indicating that the cumulative inflow equals the cumulative outflow at those points. Volume conservation is also verified by observing that the net difference between the inlet and outlet accumulated volumes returns to zero at the end of each actuation cycle. This behavior confirms that the total volume entering the chamber during a cycle is equal to the total volume exiting it, with no net accumulation. The long-term convergence of the inlet and outlet curves substantiates the physical consistency of the simulation and the micropump's ability to maintain balanced and repeatable fluid transport under cyclic operation.

3-3- Effect of piezoelectric actuator configuration on micropump performance

A comprehensive parametric study was conducted to evaluate how variations in piezoelectric actuator design, i.e. the electric field intensity (E_0) and the number of layers (n), affect micropump performance. Layer thickness t_0 is taken to be constant of 0.1 mm for $V_0=E_0 \cdot t_0 \cdot n$. When E_0 and n were varied while maintaining a constant total voltage of 1500 V, the results revealed that increasing

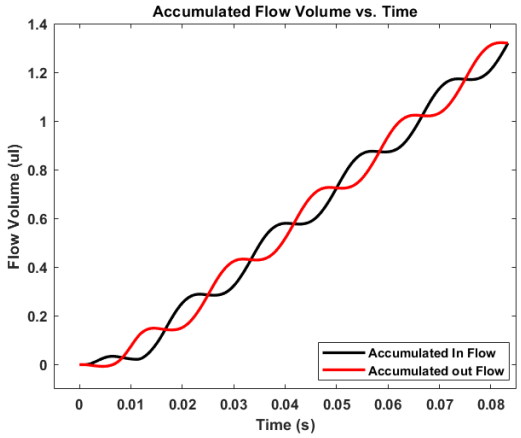

Fig. 7 Time-resolved cumulative fluid volumes at the inlet and outlet boundaries, obtained via integration of instantaneous flow rates using a global ordinary differential equation framework.

the number of layers led to significantly higher peak inlet flow rates compared to configurations with fewer layers and higher electric field intensity (Fig. 8). While a stronger electric field increases strain per layer, it does not offset the mechanical benefits of a higher layer count. A larger n increases the overall actuator thickness, thereby amplifying its stiffness and force output. This structural enhancement enables more effective membrane deformation and fluid displacement, resulting in superior pumping efficiency. Under fixed actuator

geometry (constant t_0 and n), increasing the electric field intensity E_0 directly raises the applied voltage, enhancing strain per layer, improving membrane displacement and flow rates (Fig. 9a). Conversely, when E_0 remains constant and the number of layers n increases, the resulting voltage rise is coupled with greater actuator thickness, which amplifies mechanical output and flow rates as well (Fig. 9b). This combined electrical and structural enhancement leads to a more pronounced improvement in micropump performance. So, these findings suggest that while both E_0 and n contribute to enhanced actuation, the number of layers plays a more dominant role in optimizing micropump output.

The mechanical amplification associated with increased layer count offers a more effective pathway for energy transfer and fluid displacement than simply intensifying the electric field.

Therefore, actuator designs that prioritize its thickness through higher n values are better suited for achieving high-performance micropumping.

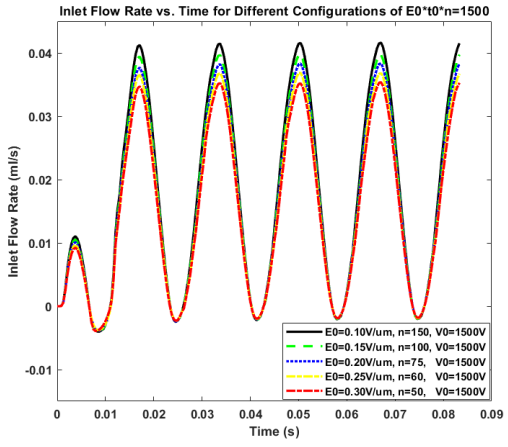

Fig. 8 Variation of inlet flow rate across piezoelectric actuator configurations under constant voltage of 1500 V, highlighting enhanced performance with increased layer count due to greater actuator stiffness and force output.

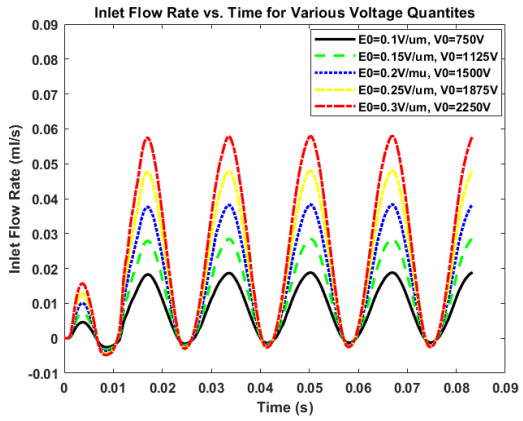

(a)

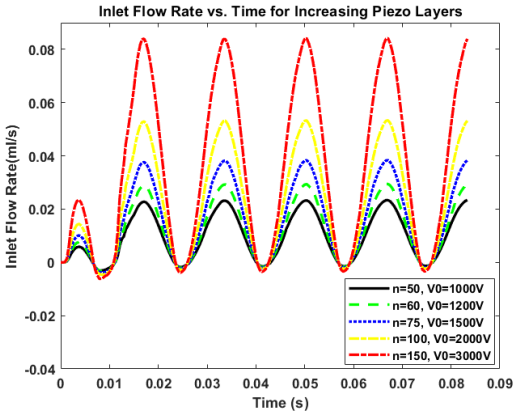

(b)

Fig. 9 Influence of electric field intensity and layer count on micropump performance. (a) Increasing E_0 under fixed actuator geometry enhances strain per layer and membrane displacement, leading to higher peak inlet flow rates, (b) Increasing n at constant E_0 raises the applied voltage and actuator thickness, resulting in stronger mechanical actuation and higher peak inlet flow rates.

It is worth considering that while increasing the applied voltage enhances membrane displacement and peak inlet flow rate, it also intensifies backflow in the inlet and outlet. Therefore, the electric field cannot be increased indefinitely, and identifying an optimal is essential for maximizing net pumping efficiency.

3-4- Increasing the inner radius of piezoelectric actuator

Increasing the inner radius of the piezoelectric actuator effectively shifts the active piezoelectric region toward the

periphery of the membrane. This geometric modification enhances the mechanical leverage by increasing the moment arm relative to the center. Consequently, the membrane experiences greater bending deformation under the same actuation voltage, leading to a higher peak displacement (Fig. 10). From a fluid dynamics standpoint, this amplified displacement induces a larger pressure differential across the pump chamber during each actuation cycle. This, in turn enhances the volumetric flow rate (Fig. 11). Moreover, this configuration reduces mechanical constraints at the membrane center. As a result, energy transfer from the piezoelectric actuator to the fluid domain becomes more efficient.

3-5- Increasing the outer radius of piezoelectric actuator

Expanding the outer radius of the piezoelectric actuator increases the total actuated area of the membrane, distributing the electromechanical force over a broader surface. Although this increases structural stiffness and reduces local bending, leading to lower peak membrane displacement (Fig. 12), the overall displaced volume per cycle still rises (Fig. 13).

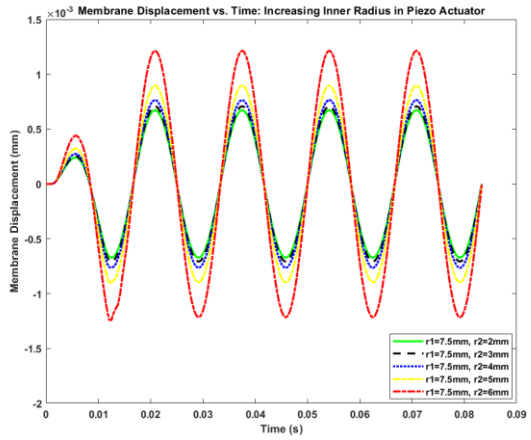

Fig. 10 Membrane displacement curves corresponding to increased inner radius of the piezoelectric actuator. Outward shift of the active region enhances mechanical leverage, resulting in greater bending deformation under constant actuation voltage.

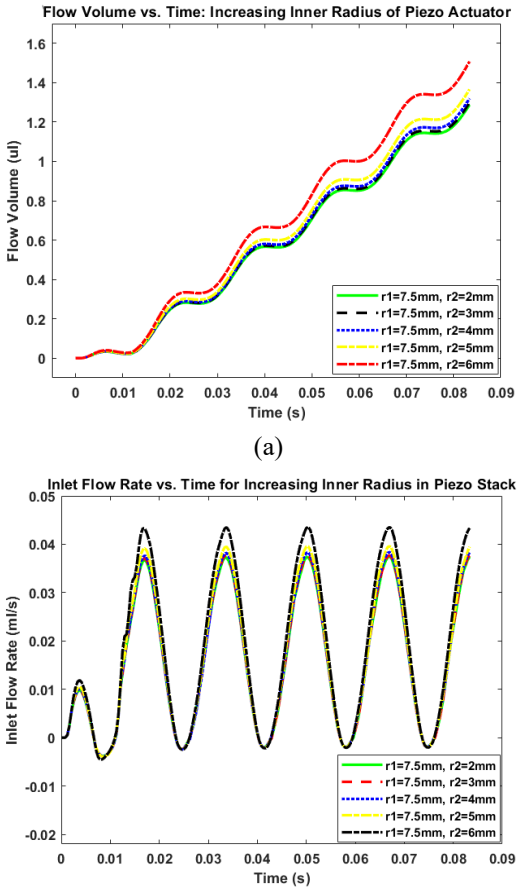

Fig. 11 Influence of inner radius of the piezoelectric actuator on flow performance. (a) Volumetric flow curves showing enhanced fluid displacement with increasing inner radius, due to amplified membrane deformation. (b) Inlet flow rate comparison for different inner radii, illustrating improved pumping efficiency as the active piezoelectric region shifts outward.

This is attributed to the larger effective area contributing to membrane motion. It compensates for the lower amplitude of deformation. Fig. 14 compares strain profiles over the membrane for piezoelectric actuators with minimum and maximum thicknesses. The broader actuation profile promotes a more uniform pressure distribution within the fluid chamber. This reduces flow resistance and enhances net fluid transport. Thus, despite reduced peak deflection, the system achieves improved pumping performance

through optimized spatial force distribution and fluid-structure interaction.

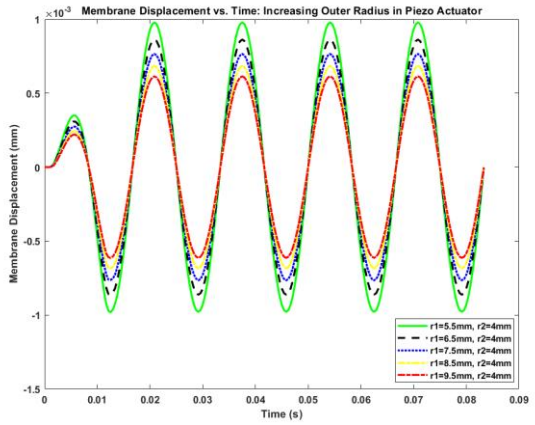

Fig. 12 Membrane displacement as a function of piezoelectric actuator outer radius. Increasing the outer radius of the piezoelectric stack reduces peak displacement due to enhanced structural stiffness and distributed actuation force.

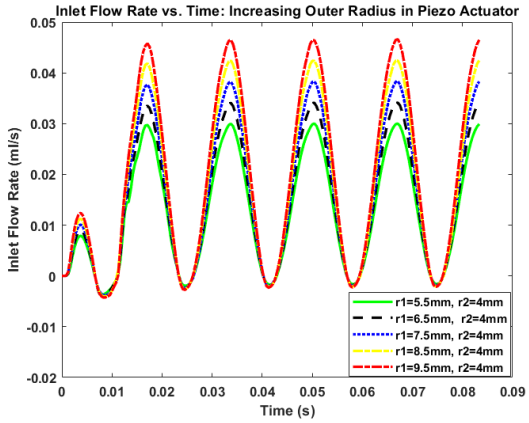

(a)

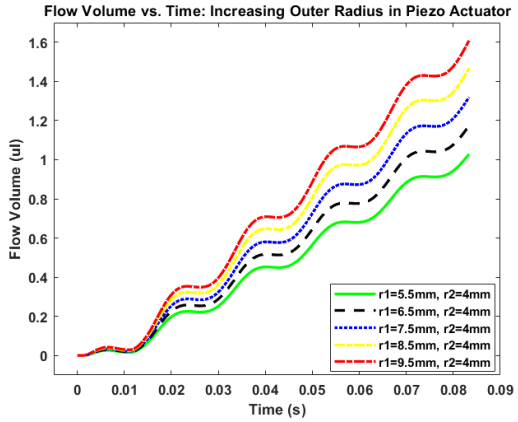

(b)

Fig. 13 Influence of the outer radius of the piezoelectric actuator on flow performance. (a) Inlet flow rate curves showing the effect of expanded actuator radius on peak flow characteristics. (b) Comparison of total volumetric flow, highlighting improved cumulative fluid volumes with increased actuated membrane area.

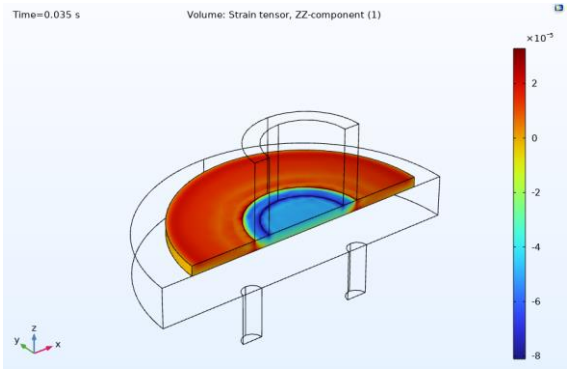

(a)

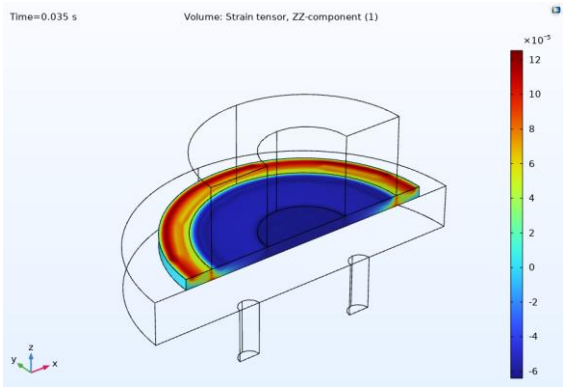

(b)

Fig. 14 Illustration of strain distribution over the membrane for the piezoelectric actuator with (a) the minimum thickness (b) the maximum thickness.

3-6- Increasing the radius of the membrane

As the membrane radius increases, the total surface area available for deformation grows quadratically. Under constant actuation voltage and frequency, the piezoelectric actuator induces a similar strain profile across the membranes of varying sizes. However, the larger membrane area converts this strain into a greater net volumetric displacement per cycle. This amplification enhances the pressure differential between the inlet and outlet channels, thereby increasing the peak inlet flow rate. Fig. 15 shows flow rates and flow volume for different membrane sizes.

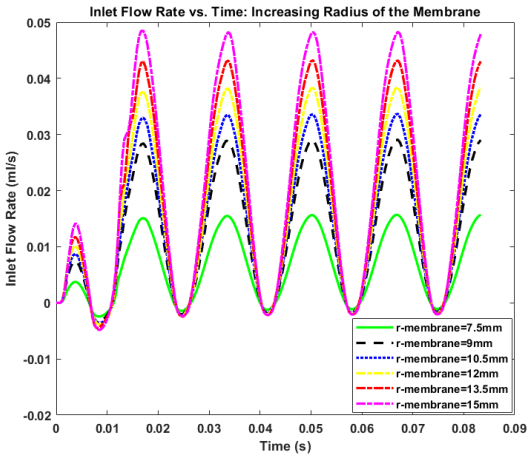

(a)

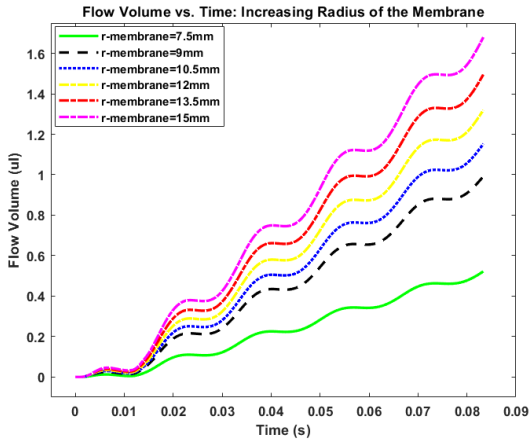

(b)

Fig. 15 Comparison of inlet flow rate profiles and cumulative volume flow for varying membrane radii under constant actuation conditions. Larger membrane sizes exhibit higher peak flow rates and increased volumetric displacement per cycle.

3-7- Increasing the radius of inlet/outlet

Simulation results reveal that increasing the inlet and outlet radii from 0.25mm to 4mm leads to a reduction in both peak inlet flow rate and total volumetric flow (Fig. 16). This behavior arises from the interplay between fluidic impedance, pressure wave propagation, and valve-like rectification dynamics. Larger port radii reduce the flow resistance at the boundaries. This lowers the pressure buildup within the pump chamber during membrane actuation. As a result, the pressure differential driving fluid motion diminishes, leading to weaker flow peaks. Additionally, this model employs a velocity-dependent boundary condition to simulate valve-like effects. With larger ports, the fluid velocity decreases for a given flow rate. This reduction weakens the rectification capability of the virtual valve and its effectiveness in suppressing backflow. (Fig. 16(a)). This degradation in directional control reduces net fluid displacement per cycle. Furthermore, the lower resistance at the enlarged inlet and outlet boundaries causes some energy to be lost rather than used to drive fluid forward, and ultimately reducing the total flow volume (Fig. 16(b)). These findings highlight the importance of optimizing port geometry to balance flow capacity, pressure generation and directional control.

3-8- Increasing the applied frequency

The frequency-dependent flow volume data obtained from simulation reveals a characteristic resonant behavior typical of piezoelectrically actuated microfluidic systems (Fig. 17). As the excitation frequency increases from 0.1 Hz to 940Hz, the maximum accumulated flow volume rises significantly, reaching a peak of 4.1528 µL at 940Hz.

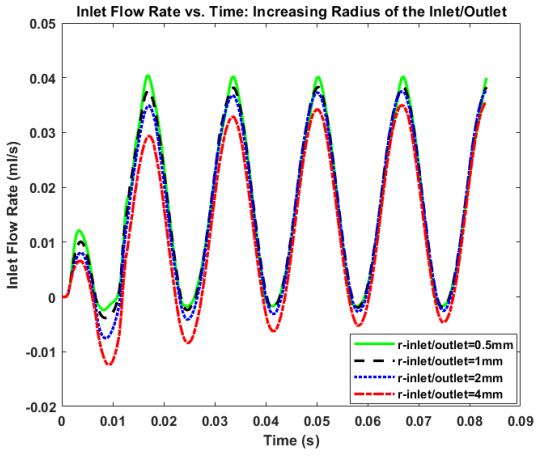

(a)

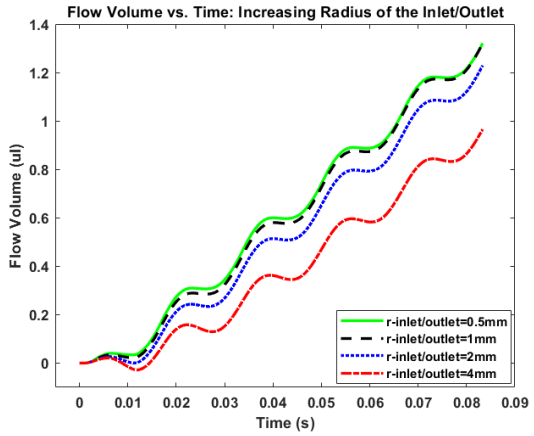

(b)

Fig. 16 Effect of port size on flow performance. Larger inlet/outlet radii reduce (a) peak flow and (b) total accumulated volume due to lower pressure buildup and weakened valving.

This peak corresponds to the system's mechanical resonance. At this point, the piezoelectric actuator undergoes maximum displacement, inducing optimal pressure gradients and fluid motion within the chamber. Beyond this frequency, the flow rate declines sharply, indicating that the system enters an off-resonance regime. At higher frequencies (1500-3000Hz), the actuator's dynamic response is limited by increased damping, reduced displacement amplitude, and phase lag between the electrical excitation and mechanical deformation. These factors diminish the efficiency of energy transfer from the actuator to the fluid, resulting in lower flow rates. The observed trend is consistent with the theoretical expectations of fluid-structure interaction in resonant micropumping systems. It validates the simulation's physical fidelity. It is worth noting that all flow rates were recorded after the same five actuation cycle for each frequency, ensuring consistent temporal resolution across the sweep.

3-9- Increasing the height of fluid chamber

When the chamber height is increased from 2mm up to 6mm, the flow rate curves remain essentially identical (Fig. 18(a)). The oscillatory peaks and troughs follow the same pattern because the membrane is exciting the same fundamental mode and viscous damping is still strong enough to limit amplitude. Also, the curves at 7mm and 8mm have the same pattern. However, the flow rate peaks rise noticeably higher. This is due to reduced viscous shear losses and increased fluid compliance, which allow the membrane to drive larger oscillatory velocities in the fluid.

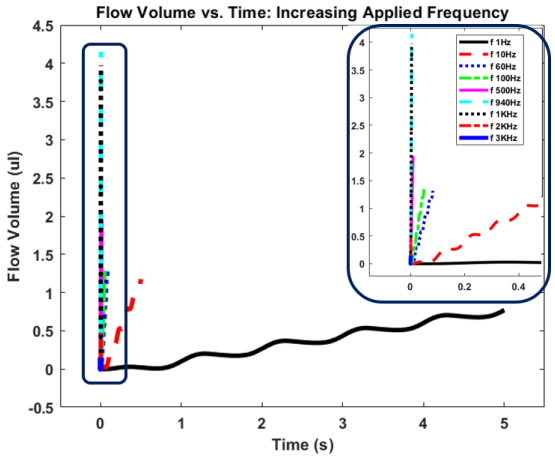

(a)

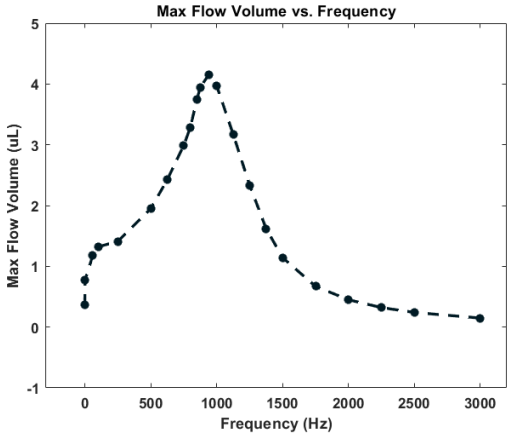

(b)

Fig. 17 (a) flow volume for the micropump at different operating frequencies. An enlarged view of the curves is shown in the upper-right inset, (b) Maximum flow volume vs. frequency. A resonant peak at 940Hz yields the maximum volume flow of 4.1528 µL. Flow decreases beyond this point due to off-resonance effects.

For 2-6 mm, the accumulated volume curves overlap almost perfectly (Fig. 18(b)), reflecting that the net pumping capacity is insensitive to modest changes in chamber height within this range. At 7-8 mm, the accumulated volume curves also overlap with each other but sit at a higher level compared to the 2-6 mm group. This indicates that the larger chamber height enables more effective energy transfer, producing greater net volume per cycle.
Thus, increasing chamber height does not alter the oscillatory dynamics of the pump but primarily scales the amplitude of both instantaneous flow rate and accumulated flow volume. This confirms that chamber height acts as a gain modifier rather than changing the underlying dynamics.

3-10- Dynamic performance analysis

In this work, the phrase Enhanced Flow Control refers to overall improvements in micropump performance achieved through structural design optimization, actuator configuration, and dynamic response analysis. While structural parameters contribute significantly to efficiency, the dynamic response provides further substantiation of enhanced control under varying operating conditions. Specifically, the pump's behavior was analyzed across a range of operating voltages and excitation frequencies. The voltage-dependent performance was presented in Section 3-3 (Figs. 8-9), where variations in electric field intensity and actuator layer count were shown to strongly influence flow rate. The frequency-dependent response was detailed in Section 3-8 (Fig. 17), where a resonance peak at 940Hz was observed, followed by off-resonance decline at higher frequencies. Together, these results demonstrate both the essential dynamic performance characteristics of the micropump and the broader improvements achieved through structural and electrical design, thereby confirming its enhanced flow control capability.

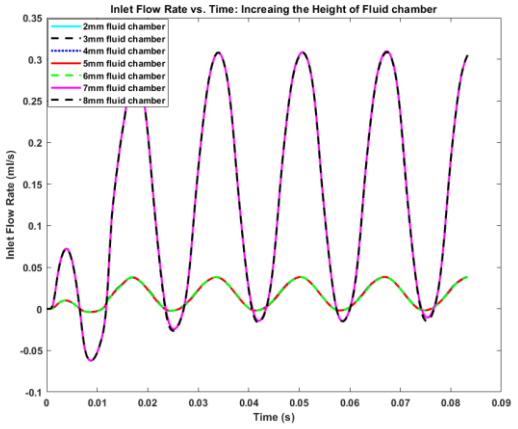

(a)

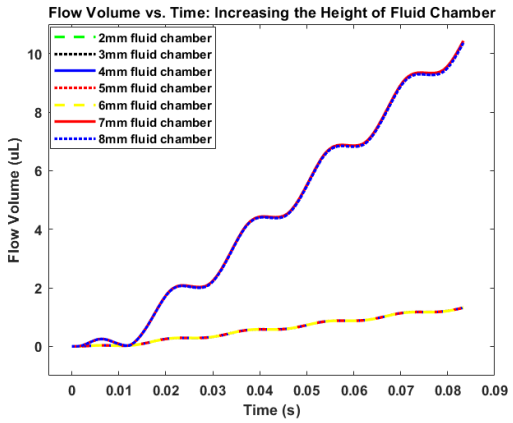

(b)

Fig. 18 Effect of chamber height on pump performance: (a) flow rate curves for chamber heights of 2-8 mm, showing identical oscillatory patterns across all cases, with noticeably higher peaks at 7-8 mm due to reduced viscous damping and increased fluid compliance, (b) accumulated flow volume curves, where 2-6 mm heights overlap almost perfectly, while 7-8 mm heights overlap at a higher level, indicating enhanced net pumping capacity per cycle.

4- Controllability of micropump performance using multiple-core configurations

This section presents a comprehensive evaluation of micropump performance across various piezoelectric actuator configurations, emphasizing how both the

number of cores and their radial arrangement influence fluid dynamics and volumetric output. Fig. 19 displays the accumulated flow volume curves for three designs: the conventional single-core actuator configuration with the ring located at radii of (4mm, 7.5mm), dual-core actuator plan with rings placement at (2mm, 5mm, 7mm, 10mm) and (3mm, 5mm, 7mm, 9mm), and triple-core actuators with rings constructed at (2mm, 4mm, 6mm, 8mm, 10mm, 12mm) and (3mm, 5mm, 7mm, 9mm, 11mm). The results demonstrate that actuator placement strongly affects pumping efficiency. For instance, the dual-core setup with rings at (2mm, 5mm, 7mm, 10mm) generates higher volumetric flow compared to the (3mm, 5mm, 7mm, 9mm) arrangement, indicating that radial positioning of actuators plays a critical role in optimizing membrane performance and fluid displacement. Similarly, the triple-core arrangement with rings at (1mm, 3mm, 5mm, 7mm, 9mm, 11mm) achieves greater flow volume than the evenly spaced configuration at (2mm, 4mm, 6mm, 8mm, 10mm, 12mm). Notably, the dual-core configuration (2mm, 5mm, 7mm, 10mm) achieves flow rates comparable to the triple-core design (2mm, 4mm, 6mm, 8mm, 10mm, 12mm), despite having fewer actuators. This finding, highlights that an optimized geometric distribution can compensate for lower actuator density, maximizing energy transfer to the fluid while minimizing destructive interference. Fig. 20 presents velocity field profiles for all tested designs at the time point corresponding to fluid exit from the outlet. These visualizations further support the flow curve analysis, showing how actuator arrangement influences velocity magnitude. Together, these results demonstrate that both actuator count and spatial arrangement are decisive factors in controlling micropump efficiency. They emphasize the importance of geometric design as a practical strategy for improving piezoelectrically actuated microfluidic systems, offering a pathway to enhanced fluid handling in lab-on-chip applications.

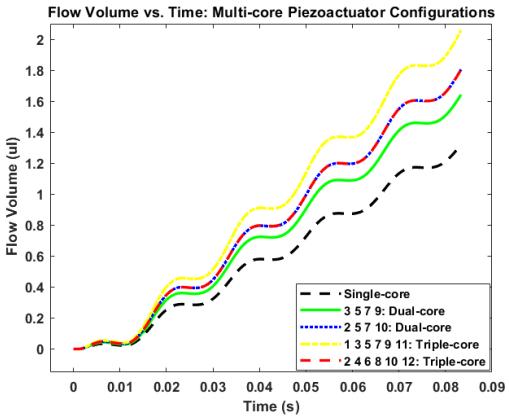

Fig. 19 Accumulated flow volume for different configurations of the piezoelectric actuator.

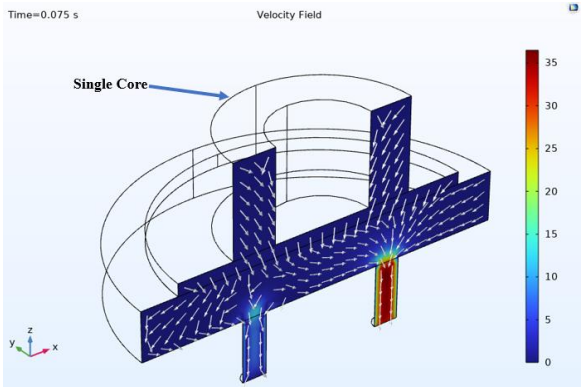

(a)

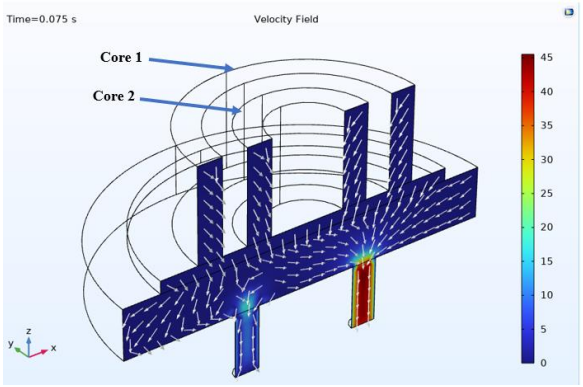

(b)

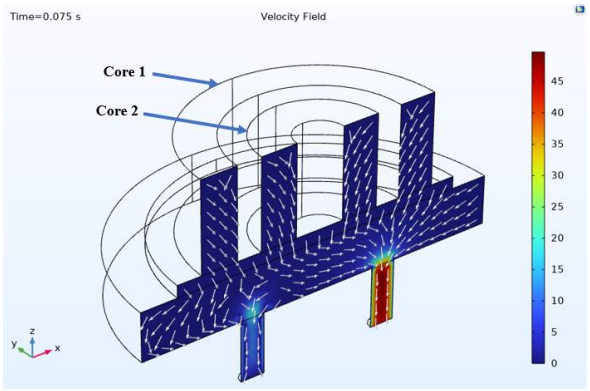

(c)

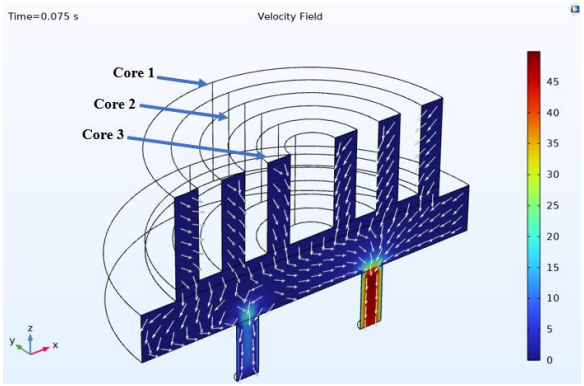

(d)

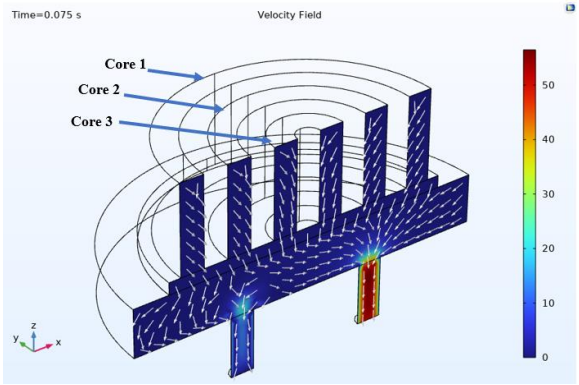

(e)

Fig. 20 Velocity filed profiles (mm/s) for (a) Single-core actuator: (radii of 4mm and 7.5mm), (b) Dual-core actuator with cores constructed at: (3mm, 5mm, 7mm, and 9mm), (c) Dual-core actuator with cores constructed at: (2mm, 5mm, 7mm, and 10mm), (d) Triple-core actuator with cores constructed at: (2mm, 4mm, 6mm, 8mm, 10mm and 12mm), and (e) Triple-core actuator with cores constructed at: (1mm, 3mm, 5mm, 7mm, 9mm and 11mm).

5- Conclusion

This study introduced and thoroughly investigated a novel fully cylindrical piezoelectric micropump architecture, emphasizing its mechanical simplicity, fabrication compatibility, and enhanced fluidic performance. Through detailed simulations using COMSOL Multiphysics, the dynamic interaction between the piezoelectric actuator, flexible membrane, and fluid domain was analyzed under valveless operation. A comprehensive parametric framework that extends beyond current models, revealed that increasing the number of piezoelectric layers significantly improves flow rate due to enhanced mechanical stiffness and actuation force, even when the applied voltage remains constant. Adjustments to actuator geometry, such as expanding the inner and outer radii, demonstrated that mechanical leverage and spatial force distribution play critical roles in optimizing membrane deformation and net fluid displacement. Similarly, increasing membrane radius amplified volumetric flow through greater surface area. In contrast, larger inlet/outlet ports reduced flow efficiency due to diminished pressure buildup and weakened rectification effects. Frequency sweep analysis identified a resonant operating point at 940Hz, where maximum flow was achieved. Beyond this frequency, performance declined due to damping and phase lag. This highlights the importance of tuning the excitation frequency to match system resonance. Additionally, multi-core actuator configurations with narrower piezoelectric rings provided a new strategy for achieving tunable and efficient flow control in valveless micropumps.

Overall, the findings provide a unique contribution for designing high-performance, valveless piezoelectric micropumps. By integrating geometric, electrical, and dynamic considerations, this work advances the development of efficient and scalable microfluidic systems

for biomedical, analytical, and industrial applications.

References

[1] Convery, N., & Gadegaard, N. (2019). 30 years of microfluidics. *Micro and Nano Engineering*, *2*, 76–91.

[2] Laser, D. J., & Santiago, J. G. (2004). A review of micropumps. *Journal of Micromechanics and Microengineering*, *14*, 35–64.

[3] Baghoolizadeh, M., Pirmoradian, M., Sajadi, S. M., Salahshour, S., & Baghaei, S. (2024). Prediction and extensive analysis of MWCNT-MgO/oil SAE 50 hybrid nano-lubricant rheology utilizing machine learning and genetic algorithms to find ideal attributes. *Tribology International*, *195*, 109582.

[4] Zhang, L., Sha, W., Li, Y., Wang, Y., & Chen, H. (2025). High-precision transdermal drug delivery enabled by a dual-pump parallel valveless piezoelectric micropump integrated with hollow microneedles. *Microsystems & Nanoengineering*, *11*, 157.

[5] Gharib, G., Bütün, İ., Muganlı, Z., Kozalak, G., Namlı, İ., et al. (2022). Biomedical applications of microfluidic devices: A review. *Biosensors*, *12*(11), 1023.

[6] Asadi Dereshgi, H., & Yildiz, M. Z. (2018). Investigation of electromechanical factors affecting piezoelectric actuator for valveless micropump characteristics. *Journal of Engineering Science and Technology*, *13*(9), 2843–2856.

[7] Asadi Dereshgi, H., Yildiz, M. Z., & Parlak, N. (2020). Performance comparison of novel single and bi-diaphragm PZT-based valveless micropumps. *Journal of Applied Fluid Mechanics*, *13*, 401–412.

[8] Mohith, S., Karanth, P. N., & Kulkarni, S. M. (2019). Recent trends in mechanical micropumps and their applications: A review. *Mechatronics*, *60*(1), 34–55.

[9] Wang, Y. N., & Fu, L. M. (2018). Micropumps and biomedical applications- A review. *Microelectronic Engineering*, *195*(1), 121–138.

[10] Liu, X., Li, X., Wang, M., Cao, S., Wang, X., et al. (2022). A high-performance piezoelectric micropump with multi-chamber in series. *Applied Sciences*, *12*(9), 4483.

[11] Haldkar, R. K., Khalatkar, A., Gupta, V. K., & Sheorey, T. (2021). New piezoelectric actuator design to enhance the micropump flow. *Materials Today: Proceedings*, *44*, 776–781.

[12] Munas, F. R., Amarasinghe, Y. W. R., & Dao, D. (2015). Review on MEMS-based micropumps for biomedical applications. *International Journal of Innovative Research in Science, Engineering and Technology*, *4*(7), 5602–5615.

[13] Yildiz, M. Z., & Dereshgi, H. A. (2019). Design and analysis of PZT micropumps for biomedical applications: Glaucoma treatment. *Journal of Engineering Research*, *7*(2), 202-217.

[14] Dong, J., Cao, Y., Chen, Q., Liu, H., & Zhang, T. (2020). Performance of single piezoelectric vibrator micropump with check valve. *Journal of Intelligent Material Systems and Structures*, *31*, 117–126.

[15] Haldkar, R. K., Gupta, V. K., & Sheorey, T. (2017). Modeling and flow analysis of piezoelectric-based micropump with various shapes of microneedle. *Journal of Mechanical Science and Technology*, *31*, 2933–2941.

[16] Asadi Dereshgi, H., Dal, H., & Yildiz, M.Z. (2021). Piezoelectric micropumps: state of the art review. *Microsystem Technologies*, *27*, 4127–4155.

[17] Hasan, M. I., Ali, A. J. F., & Tufah, R. S. (2017). Numerical study of the effect of channel geometry on the performance of magnetohydrodynamic micropump. *Engineering Science and Technology, an International Journal*, *20*(3), 982–989.

[18] He, X., Xu, W., Lin, N., Zhang, Y., & Chen, L. (2017). Dynamics modeling and vibration analysis of a piezoelectric diaphragm applied in valveless micropump. *Journal of Sound and Vibration*, *405*, 133–143.

[19] Hu, Y., You, H., & Wang, W. (2017). Non-linear deflection of a circular diaphragm-type piezoactuator under loads of voltage and pressure. *Sensors and Actuators A: Physical*, *268*, 91–100.

[20] Ma, H. K., Chen, R. H., Yu, N. S., & Hsu, Y. H. (2016). A miniature circular pump with a piezoelectric bimorph and a disposable chamber for biomedical applications. *Sensors and Actuators A: Physical*, *251*, 108–118.

[21] Ma, T., Sun, S., Li, B., & Chu, J. (2019). Piezoelectric peristaltic micropump integrated on a microfluidic chip. *Sensors and Actuators A: Physical*, *292*, 90–96.

[22] Bußmann, A., Leistner, H., Zhou, D., Wackerle, M., Congar, Y., et al. (2021). Piezoelectric silicon micropump for drug delivery applications. *Applied Sciences*, *11*(17), 8008.

[23] Tian, X., Wang, H., Wang, H., Wang, Z., Sun, Y., et al. (2021). Design and test of a piezoelectric micropump based on hydraulic amplification. *AIP Advances, 11*(6), 065230.

[24] Chen, X., Chen, Z., Gui, Z., Zhang, F., Zhang, W., et al. (2021). A novel valve-less piezoelectric micropump generating recirculating flow. *Engineering Applications of Computational Fluid Mechanics, 15*(1), 1473–1490.

[25] Peng, Y.-H., & Wang, D.-H. (2022). A novel multi-channel silicon-based piezoelectric micropump with active piezoelectric valve array. *Smart Materials and Structures, 31*(7), 075010.

[26] Ji, J., Chen, S., Xie, X., Wang, X., Kan, J., et al. (2019). Design and experimental verification on characteristics of valve-less piezoelectric pump affected by valve hole spacing. *IEEE Access*, *7*, 36259-36265.

[27] Dereshgi, H. A., & Yildiz, M. Z. (2018). Investigation of electro-mechanical factors affecting piezoelectric actuator for valveless micropump characteristics. *Journal of Engineering Science and Technology*, *13*(9), 2843–2856.

[28] Farshchi Yazdi, S. A. F., Corigliano, A., & Ardito, R. (2019). 3-D design and simulation of a piezoelectric micropump. *Micromachines*, *10*(4), 259.

[29] Revathi, S., & Padmanabhan, R. (2018). Design and development of piezoelectric composite-based micropump. *Journal of Microelectromechanical Systems*, *27*(6), 1105–1113.

[30] Bonk, S. M., Stubbe, M., Buehler, S. M., Tautorat, C., Baumann, W., et al. (2015). Design and characterization of a sensorized microfluidic cell-culture system with electro-thermal micro-pumps and sensors for cell adhesion, oxygen, and pH on a glass chip. *Biosensors*, *5*(3), 513-536.

[31] Calderon, M., & Reyes-Betanzo, C. (2023). Design and simulation of a piezoelectric micropump for drug delivery systems. *Microsystem Technologies, 29*, 253–264.

[32] Ni, J., Xuan, W., Li, Y., Chen, J., Li, W., et al. (2023). Analytical and experimental study of a valveless piezoelectric micropump with high flowrate and pressure load. *Microsystems & Nanoengineering, 9*, 72.

[33] Fan, Y., Zhang, X., Xing, G., Xiang, L., Hu, R., et al. (2023). A high flow rate piezoelectric micropump for miniature liquid cooling system. *In Proceedings of the 2023 IEEE 25th Electronics Packaging Technology Conference (EPTC), IEEE*.

[34] Ghaemi, A., Ebrahimi, A., & Hajipour, M. (2024). Integrated multiphysics modeling of a piezoelectric micropump. *In Proceedings of the 22nd International Conference of Iranian Aerospace Society. Iranian Aerospace Society*.

[35] Singh, N. S. S., Hassan, W. H., Ahmed, Z. M. A., Al-zahy, Y. M. A., Salahshour, S., & Pirmoradian, M. (2025). Non-local piezoelasticity to incorporate the influence of small-scale factors on the resonance behavior of the Mindlin piezoelectric polymeric nanoplates. *Case Studies in Chemical and Environmental Engineering*, *11*, 101125.

[36] Nabifar Khafri, A., & Bayareh, M. (2024). Numerical simulation of a micropump based on piezoelectric actuator. *Journal of Applied and Computational Sciences in Mechanics*, *36*(3), 1–14.